Stefan flow induced natural convection suppression on high-flux evaporators

As Published: 10.1016/J.ICHEATMASSTRANSFER.2019.03.020

Publisher: Elsevier BV

Persistent URL: https://hdl.handle.net/1721.1/134828

Version: Author's final manuscript: final author's manuscript post peer review, without publisher's formatting or copy editing

International Communications in Heat and Mass Transfer 106 (xxxx) xxxx

Contents lists available at ScienceDirect

International Communications in Heat and Mass Transfer

journal homepage: www.elsevier.com/locate/ichmt

Stefan flow induced natural convection suppression on high-flux evaporators

Lenan Zhang[1], Lin Zhao[1], Evelyn N. Wang*

Department of Mechanical Engineering, Massachusetts Institute of Technology, Cambridge, MA 02139, USA

A B S T R A C T

High-flux evaporators are important for various fundamental research and industrial applications. Understanding the heat loss mechanisms, especially the contribution of natural convection during evaporation is thus a ubiquitous process to predict and optimize the performance of evaporators. However, a comprehensive analysis on natural convection heat transfer, where the vertical Stefan flow due to evaporation couples with buoyancy driven convective flow has not been carefully considered. In this work, we developed a theoretical framework to elucidate the effect of Stefan flow on natural convection during evaporation. This theory incorporates the vertical Stefan flow into the conventional boundary layer theory. We found that a significant suppression of natural convection can be induced by a weak Stefan flow owing to the increase of boundary layer thickness. To understand this phenomenon, we discuss the governing mechanisms at different Stefan flow regimes. We provide a theoretical correlation to the overall heat transfer which includes both effects of the Stefan flow velocity and the buoyancy force. We finally predict the effect of natural convection on an evaporator at different operating temperatures. The heat loss from natural convection no longer monotonically increases with the superheat temperature due to the effect of Stefan flow suppression. As a result, there is an approximately 40% overestimation of the natural convection contribution at saturation temperature using conventional theory. This work improves the fundamental understanding of the natural convection during evaporation and can help guide future high-performance evaporator designs.

1. Introduction

Recent advances in high-performance evaporators promise utilization in a variety of applications including thermal management [1–4], water purification [5,6], and steam generation [7–10]. Accurate estimation of the heat loss is critical to design, predict and optimize the performance of the evaporator. Natural convection is one of the most ubiquitous sources to the heat loss which is particularly important when the evaporator operates at high temperature (*e.g.*, the saturation temperature) or has a large characteristic length scale (Rayleigh number $Ra_L \propto L^3$) [11]. To understand this fundamental process, a number of theoretical and experimental studies have been carried out, such as natural convection on a hot/cold plate with arbitrary inclination [12–20], natural convection on objects with complex geometry [21] and natural convection on porous media [22–27].

To analyze the heat loss through natural convection on an evaporator, classical theories describing the heat transfer on a horizontal hot plate in the quiescent air ambient have been previously used [7,28]. However, the assumption of a quiescent air ambient is not necessarily true especially at high fluxes because of evaporation-induced Stefan flow, which arises from the removal of air at the liquid-vapor interface [29]. As shown in Fig. 1, diffusive transport of air and vapor occurs in the gas phase due to the presence of a concentration gradient. Since the liquid-vapor interface is considered impermeable to air molecules, an upward bulk gas flow, known as the Stefan flow (Fig. 1), must compensate the diffusive air flux and maintain the vapor pressure. Therefore, natural convection is always associated with Stefan flows during evaporation into an air ambient.

To predict the heat loss on evaporators accurately, it is crucial to understand the effect of Stefan flow on natural convection. In this work, we performed theoretical analysis on natural convection with Stefan flow in ambient air. We developed an analytical model using boundary layer theory. We found heat transfer through natural convection can be significantly suppressed even when the Stefan flow is much weaker than the buoyancy-induced flow. More than 50% reduction of the Nusselt number was found at moderate bulk flow velocities (*e.g.*, ~0.01 m/s). This suppression effect is very sensitive to the geometric configurations and the wall superheat temperature of the evaporator. We finally applied the proposed theory to a device-level analysis. We calculated the natural convection-induced heat loss and analyzed the corresponding dominant mechanisms at different superheat temperatures. We found the contribution of natural convection to total heat loss can be overestimated by over 40% at high superheat temperatures if the effect of Stefan flow is ignored. The physical insights explored in this work enhance the mechanistic understanding of natural convection in the presence of Stefan flow. In addition, the proposed theory serves as a

* Corresponding author.
E-mail address: enwang@mit.edu (E.N. Wang).
[1] Equal contribution to this work.

https://doi.org/10.1016/j.icheatmasstransfer.2019.03.020

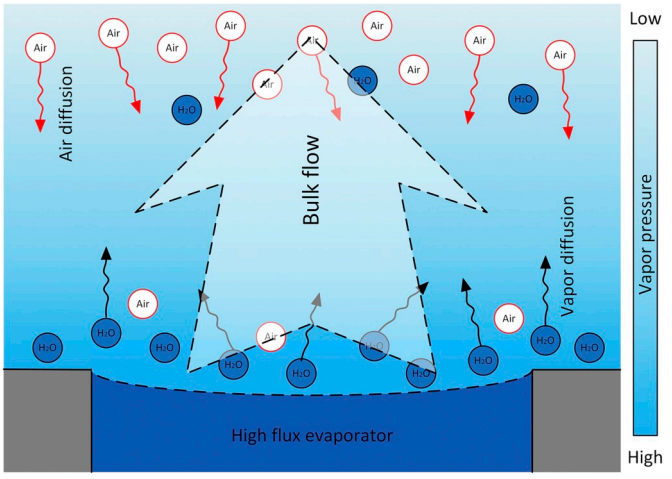

Fig. 1. Schematic of the evaporation induced Stefan flow on the liquid-vapor interface at high evaporative flux. During evaporation, air molecules transport downwards due to the presence of a concentration gradient. As the liquid-vapor interface is impermeable to air molecules, an upward Stefan flow forms to maintain the vapor pressure at the interface.

new tool to analyze the heat loss and aid in the design of high-performance evaporators.

2. Theoretical formulation

2.1. Boundary layer theory of natural convection in a Stefan flow

We first applied boundary layer theory to study the effect of Stefan flow on natural convection analytically. We considered a two-dimensional, steady, laminar boundary layer on a horizonal evaporator. As many high-performance evaporators are operated in a planar configuration [4,28,30], we modeled the evaporator as a semi-infinite flat hot plate with a uniform temperature T_s and the half length of L. To further simplify the problem, we made the following assumptions: (1) The Stefan flow velocity V_0 is reasonably small compared to the horizontal characteristic velocity U so that the boundary layer assumption is still valid. (2) No-slip boundary condition can be applied to the air flow at the liquid-vapor interface as the dynamic viscosity of liquid water is one order of magnitude larger than that of the air (*e.g.*, 8.9×10^{-4} $Pa \cdot s$ compared to 1.8×10^{-5} $Pa \cdot s$ at 25°C, respectively). For evaporators that use micro/nano structures or pores where a large portion of them is covered by solid, this assumption more strictly holds [4,28] (Fig. 2). (3) All of the fluid properties are assumed to be constant except for the air density, which is described by the Boussinesq approximation. These fluid properties were evaluated at $T_f = (T_s + T_\infty)/2$. (4) The viscous and thermal boundary layer have the same thickness $\delta(x)$ because the Prandtl number $Pr \leq 1$ [11]. As shown in Fig. 2, we focus on solving the boundary layer problem in region I (the boundary layer in region II is also solved in Appendix C). For convenience, we set the origin of the coordinate system at the leading edge of the plate. We obtain the governing equations for the natural convection boundary layer in the Stefan flow using a scaling analysis (Appendix A for detailed derivations),

$$\frac{\partial u}{\partial x} + \frac{\partial v}{\partial y} = 0 \tag{1}$$

$$\rho\left(u\frac{\partial u}{\partial x} + v\frac{\partial u}{\partial y}\right) = -\frac{\partial p}{\partial x} + \mu\frac{\partial^2 u}{\partial y^2} \tag{2}$$

$$\rho_\infty(1 - \beta(T - T_\infty))g = -\frac{\partial p}{\partial y} \tag{3}$$

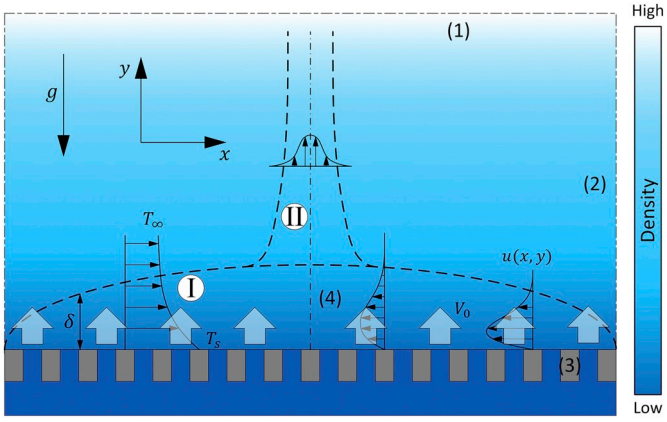

Fig. 2. Schematic of the natural convection boundary layer on the evaporator. Uniform Stefan flow V_0 is applied on the interface. Natural convection occurs in the gas phase due to the presence of a density gradient. In region I, the flow and thermal boundary layers cover the top of the evaporator with temperature T_s. The boundary layer thickness δ varies along x direction. A uniform upward flow V_0 enters region I through the interface. At the center of the evaporator, the fluid flow leaves region I and moves upwards into region II, where a vertical boundary forms. The computational domain is defined by four boundaries. Boundary (1) indicates the far-field condition, where the ambient temperature and pressure is applied. Boundary (2) is at the leading edge of the evaporator. Boundary (3) is located at the interface, where the temperature and upward flow velocity are defined by T_s and V_0, respectively. A no-slip boundary condition is applied to the horizontal flow. The evaporator is symmetric about the axis (4).

$$u\frac{\partial T}{\partial x} + v\frac{\partial T}{\partial y} = \alpha\frac{\partial^2 T}{\partial y^2}. \tag{4}$$

The boundary conditions are,

$$u = 0,\ v = V_0,\ T = T_s, \quad \text{at } y = 0 \tag{5}$$

$$u = 0,\ T = T_\infty,\ p = p_\infty, \quad \text{at } y \to \infty \tag{6}$$

where u and v are the flow velocity in x- and y-direction, respectively. T and p are the temperature and pressure. ρ, μ, and α are the gas density, viscosity and thermal diffusivity, respectively. We use the well-known approximate expressions for the velocity and temperature profile within the boundary layer which automatically satisfy the boundary conditions (Eqs. (5) and (6)) [20],

$$u(x,y) = U(x)\frac{y}{\delta(x)}\left(1 - \frac{y}{\delta(x)}\right)^2 \tag{7}$$

$$\frac{T(x,y) - T_\infty}{T_s - T_\infty} = \left(1 - \frac{y}{\delta(x)}\right)^2. \tag{8}$$

We combine the x- and y-momentum equations (Eqs. (2) and (3)) by substituting the pressure gradient term,

$$\rho\left(u\frac{\partial u}{\partial x} + v\frac{\partial u}{\partial y}\right) = \rho_\infty\beta g\int_y^\infty \frac{\partial}{\partial x}(T - T_\infty)dy + \mu\frac{\partial^2 u}{\partial y^2}. \tag{9}$$

Combining the continuity equation (Eq. (1)) with the momentum (Eq. (9)) and the energy equation (Eq. (4)) and integrating them within the boundary layer, we obtain

$$\frac{d}{dx}\int_0^\delta u^2 dy = g\beta\int_0^\delta\int_y^\infty \frac{\partial}{\partial x}(T - T_\infty)dydy - \nu\frac{\partial u}{\partial y}\bigg|_{y=0} \tag{10}$$

$$\frac{d}{dx}\int_0^\delta u(T - T_\infty)dy = V_0\Delta T - \alpha\frac{\partial T}{\partial y}\bigg|_{y=0} \tag{11}$$

where $\Delta T = T_s - T_\infty$ is the wall superheat. Note, except the term $V_0\Delta T$, Eqs. (10) and (11) have the same expression as the momentum and

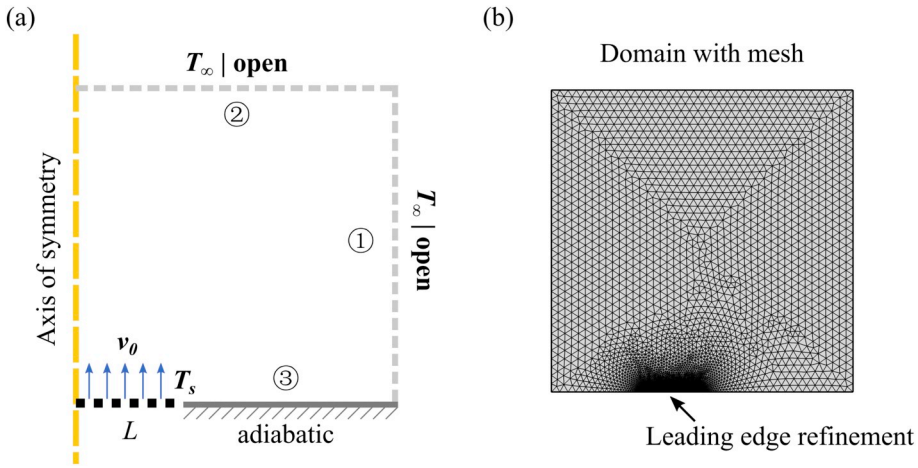

Fig. 3. (a) Simulation domain with boundary conditions. The evaporator of length L is indicated by the black dotted line. Boundary 1 and 2 are open boundaries to allow air to flow into the domain. Boundary 3 near the leading edge of the evaporator is modeled as adiabatic. (b) Simulation domain with mesh. Boundary conditions applied in this simulation are the same as the conditions described in Fig. 2. The mesh near the leading edge of the evaporator is refined by a factor of 100.

energy integral for conventional boundary layer theory because the governing equations (Eqs. (1)–(4)) for both conditions are the same. $V_0\Delta T$ indicates the Stefan flow effect due to the boundary condition $v = V_0$ at $y = 0$. Substituting the velocity and temperature profile (Eqs. (7) and (8)) into the integral equations (Eqs. (10) and (11)), we obtain the equations for the natural convective boundary layer in Stefan flows,

$$\frac{1}{105}\frac{d}{dx^*}(U^{*2}\delta^*) = -\frac{U^*}{\delta^*} + Gr_L\delta^*\frac{d\delta^*}{dx^*} \tag{12}$$

$$\delta^*\frac{d}{dx^*}(U^*\delta^*) = 30Re_{V_0}\delta^* + \frac{60}{Pr} \tag{13}$$

where $x^* = x/L$, $\delta^* = \delta/L$ and $U^* = UL/\nu$ are the dimensionless forms of corresponding variables. Gr_L is the Grashof number, *i.e.*, $Gr_L = \frac{g\beta\Delta TL^3}{\nu^2}$, and $Re_{V_0} = \frac{V_0L}{\nu}$ is the Stefan flow Reynolds number. Physically, Eq. (12) indicates the balance between inertial ($\frac{1}{105}\frac{d}{dx^*}(U^{*2}\delta^*)$), viscous ($-\frac{U^*}{\delta^*}$) and buoyant ($Gr_L\delta^*\frac{d\delta^*}{dx^*}$) forces, and Eq. (13) demonstrates the energy balance between horizontal convection ($\delta^*\frac{d}{dx^*}(U^*\delta^*)$), vertical convection ($30Re_{V_0}\delta^*$), and conduction ($60/Pr$). According to Eqs. (12) and (13), the average Nusselt number of natural convection $\overline{Nu_L}$ is determined by Gr_L, Re_{V_0}, and Pr, *i.e.*, $\overline{Nu_L} = \overline{Nu_L}(Gr_L, Re_{V_0}, Pr)$. Eqs. (12) and (13) can be solved strictly using numerical methods. In addition, we can also find the analytical solution with proper approximations, which shows more physical insights into the dominant mechanism of heat transfer (Appendix B for detailed derivations). To predict the overall heat transfer through natural convection, we calculate the average Nusselt number $\overline{Nu_L}$ as,

$$\overline{Nu_L} = \int_0^1 \frac{2}{\delta^*}dx^*. \tag{14}$$

2.2. Finite element simulation of natural convection in a Stefan flows

To more accurately obtain the evolution of the boundary layer, we also carried out numerical simulations based on the finite element method (FEM) using COMSOL. Similar assumptions used in the boundary layer approach (*e.g.,* constant fluid properties and the Boussinesq approximation) were incorporated in the FEM simulations. The two-dimensional simulation domain is shown in Fig. 3(a), which consists of the evaporator and the air ambient surrounding it. The evaporator is modeled as a long strip in the third dimension (into the page), similar to the boundary layer theory. Because of symmetry, only half of the domain is included, with the axis of symmetry at the center plane of the evaporator. The length of the evaporator in the domain is L (*i.e.*, the full evaporator length is $2L$) and the overall size of the simulation domain is $2.5L$ by $2.5L$. Boundaries 1 and 2 are defined as open boundaries to allow air to enter (at temperature T_∞) and exit the domain freely. Boundary 3 in front of the leading edge of the evaporator is modeled as an adiabatic wall. Because most of the heat transfer occurs near the leading edge of the infinite strip, it is important to resolve the flow accurately in that area. We applied a refined mesh near the leading edge as shown in Fig. 3(b). The refinement factor as well as the overall domain size were determined such that further increasing them does not appreciably change the results (relative change < 0.5%, Appendix D for details). In a typical simulation, the fluid velocity field and temperature field were calculated at incremental time steps until they reached their steady state after the initial disturbance decayed.

2.3. Theory of one-dimensional Stefan flow on an evaporator

The vapor transport during evaporation is usually modeled by Fick's law [29], where vapor molecules diffuse upwards while air molecules diffuse downwards due to a concentration gradient. However, as the liquid interface is impermeable to air, an upward bulk flow (*i.e.*, Stefan flow) is required to balance the downward diffusive flux of air molecules with velocity V_0 such that the net air flux (convective plus diffusive) is zero at the interface (Fig. 1). This bulk flow is no longer negligible as the evaporative flux increases where the dilute-solution assumption of Fick's law starts to break down. Therefore, we modeled the vapor transport using the Maxwell-Stefan law instead, where the bulk flow velocity is given by,

$$V_0 = \frac{D}{p_A}\frac{dp_A}{dy} \tag{15}$$

where D is the mass diffusivity, and p_A is the partial pressure of air. Accordingly, this bulk air-vapor flow creates a convective vapor flux, *i.e.*, $\frac{p_vM_v}{R_0T}V_0$. Combining the convective and the diffusive flux, the total vapor flux j is expressed as,

$$j = -\frac{DM_v}{R_0T}\frac{dp_v}{dy} + \frac{p_vM_v}{R_0T}V_0 \tag{16}$$

where M_v is water molecular weight, R_0 is the universal gas constant and p_v is the vapor partial pressure. Using Eq. (15) as well as the facts that $p_v + p_A = p_\infty$ and $dp_v/dy + dp_A/dy = 0$, we can obtain the total vapor flux j as,

Table 1
Parameters for natural convection heat transfer calculation in a quiescent air ambient.

T_s	T_∞	L	Pr	Gr_L
40°C	25°C	1–20 cm	0.706	10^3–10^7

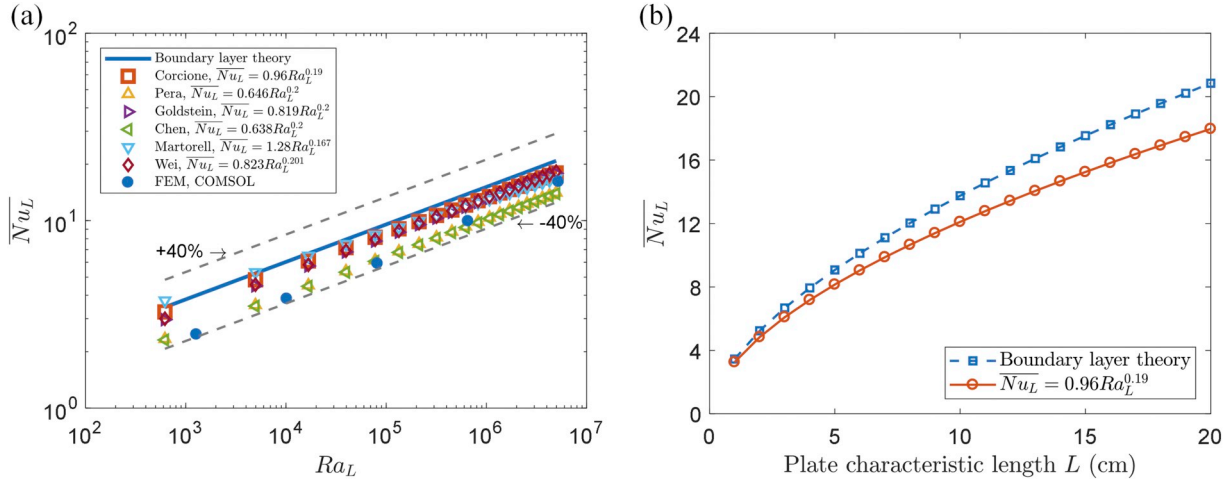

Fig. 4. Comparison between the present theory and the suggested correlations. Both the boundary layer theory solution and the FEM results agree with the widely used correlations well. The deviation between the theory and correlation increases as the plate characteristic length increases.

Table 2
Parameters for natural convection heat transfer calculation with different Stefan flow Reynolds numbers.

T_s	T_∞	L	Pr	Gr_L	Re_{V_0}
40°C	25 °C	5 cm	0.706	10^5	0–240

$$j = \frac{DM_v p_\infty}{R_0 T p_A}\frac{dp_A}{dy} \tag{17}$$

where Eq. (17) is known as the Stefan's law and can be integrated to give,

$$j = \frac{DM_v p_\infty}{R_0 T \delta_c}\ln\frac{p_\infty - p_{v,\infty}}{p_\infty - p_{v,s}}. \tag{18}$$

Here δ_c represents the effective boundary layer thickness which is typically scaled by the characteristic length L of the evaporator and is determined experimentally in practice [28]. By substituting the unknown pressure gradient in Eq. (15) using Eqs. (17) and (18), we obtained the final form of V_0 as,

$$V_0(T_s, T_\infty) = \frac{D}{\delta_c}\ln\frac{p_\infty - p_{v,\infty}(T_\infty)}{p_\infty - p_{v,s}(T_s)} \tag{19}$$

which is a function of the evaporator temperature T_s and air ambient temperature T_∞.

3. Results and discussion

3.1. Method assessment

To validate our method, we calculated the natural convection in a quiescent air ambient and compared the results with well-known correlations. The simulation parameters are given in Table. 1. As shown in Fig. 4(a), both the boundary layer solution and the FEM results agree well with the experimental correlations. Specifically, the boundary layer solution (*i.e.*, $\overline{Nu_L} = 0.98Ra_L^{0.2}$) shows excellent agreement with the correlation suggested by Corcione (*i.e.*, $\overline{Nu_L} = 0.96Ra_L^{0.19}$) and reasonable agreement with other commonly used correlations (< 40% deviation) within the range of Ra_L (*i.e.*, $10^4 < Ra_L < 10^7$) that the correlations are valid [31]. The FEM results generally predict the overall heat transfer to be lower than the boundary layer solution because: (1) FEM has a larger numerical error at the leading edge due to

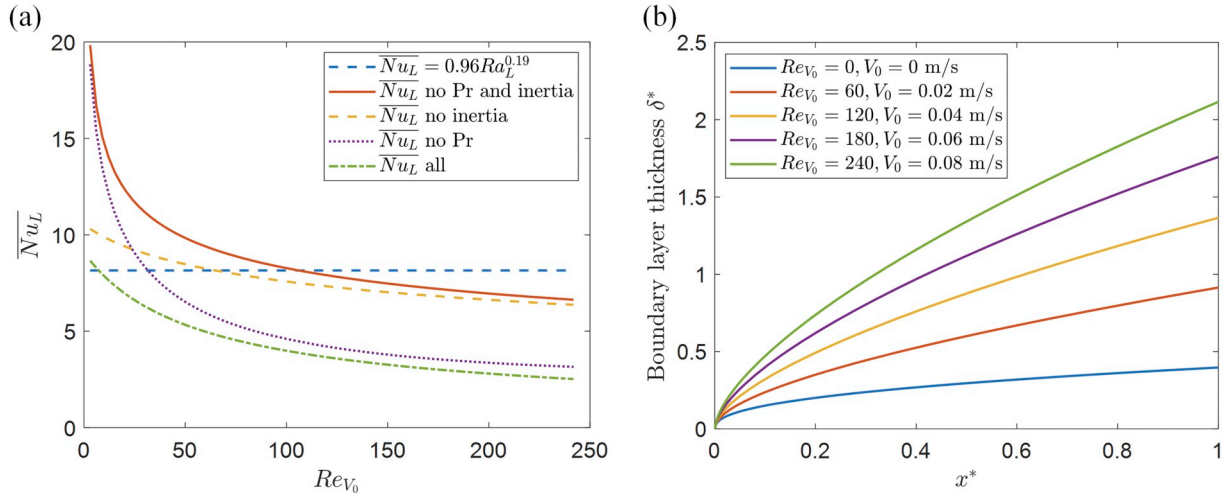

Fig. 5. Effect of Stefan flow on the heat transfer through natural convection and the boundary layer thickness. (a) The average Nusselt number $\overline{Nu_L}$ as a function of Stefan flow Reynolds number Re_{V_0}. The average Nusselt number $\overline{Nu_L}$ decreases rapidly when a weak Stefan flow occurs ($Re_{V_0} < 90$) (b) The boundary layer thickness as a function of x-coordinate under different Stefan flow velocities. The decrease of overall heat transfer performance arises from the increase of boundary layer thickness in the Stefan flow.

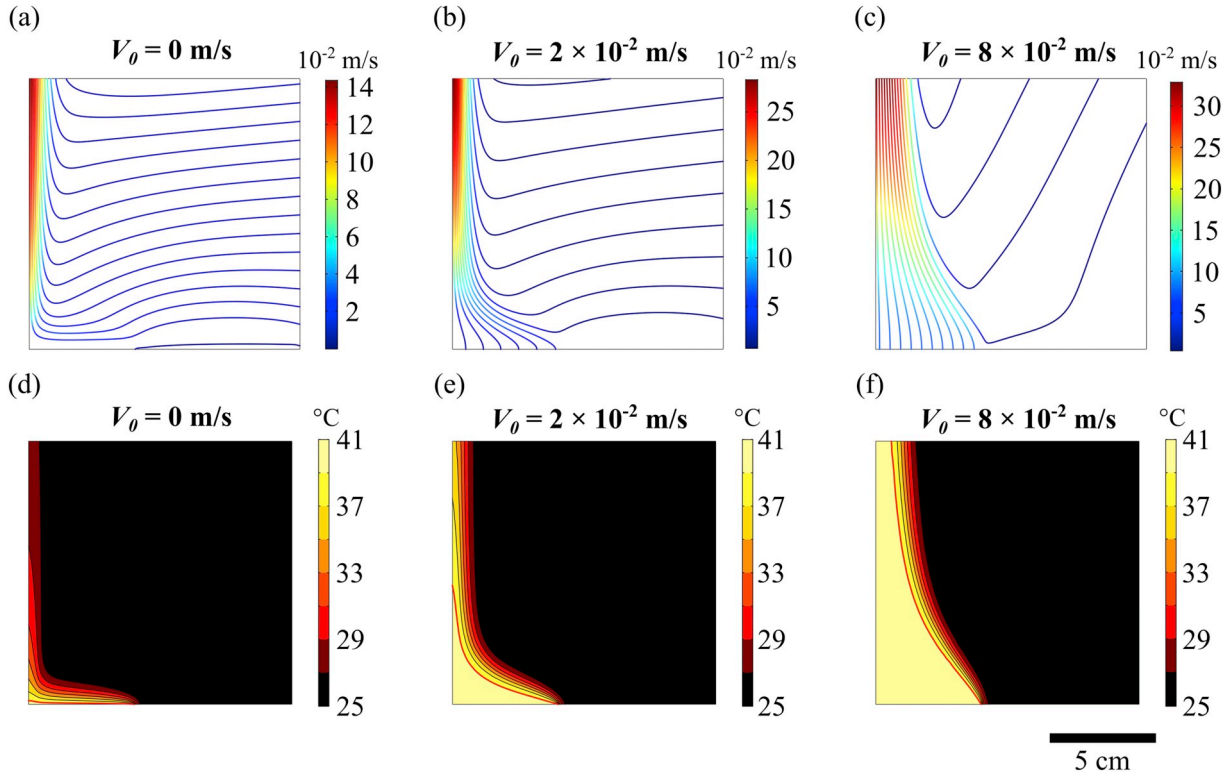

Fig. 6. FEM simulation results of the velocity field when (a) $V_0 = 0$ m/s ($Re_{V_0} = 0$), (b) $V_0 = 0.02$ m/s (Re_{V_0}~60) and (c) $V_0 = 0.08$ m/s (Re_{V_0}~240), and the temperature distribution when (d) $V_0 = 0$ m/s ($Re_{V_0} = 0$), (e) $V_0 = 0.02$ m/s (Re_{V_0}~60) and (f) $V_0 = 0.08$ m/s (Re_{V_0}~240). The red line in (d)-(f) represents an isotherm of $T = 39$ °C, which demonstrates the evolution of boundary layer thickness. (For interpretation of the references to colour in this figure legend, the reader is referred to the web version of this article.)

the limited refinement (Fig. A2, Appendix E), and (2) the heat transfer in region II (Fig. 2) cannot be well-described by the boundary layer theory (Appendix E for details). Fig. 4(b) shows that the boundary layer theory deviates from the experimental correlation $\overline{Nu_L} = 0.96Ra_L^{0.19}$ more significantly at a larger characteristic length L. One of the possible reasons is that at large L, flow instability usually occurs for which reason the steady laminar boundary layer assumption cannot strictly hold [32,33].

3.2. Effect of Stefan flow on natural convection

To understand the effect of Stefan flow, we studied natural convection at a variety of vertical flow velocities ranging from 0 to 0.08 m/s where the corresponding Stefan flow Reynolds number Re_{V_0} ranges from 0 to 240. We investigated natural convection on a two-dimensional evaporator with $L = 5$ cm. The simulation parameters are listed in Table 2.

Fig. 5(a) shows the average Nusselt number $\overline{Nu_L}$ of natural convection varies with Re_{V_0}. The natural convection heat transfer decreases significantly as the increase of Stefan flow velocity, indicating the heat loss through natural convection is heavily suppressed by Stefan flow. Particularly, $\overline{Nu_L}$ decreases > 50% when V_0 rises to 0.03 m/s (*i.e.*, $Re_{V_0} = 90$). Note that $V_0 = 0.03$ m/s is much smaller than the characteristic vertical velocity $V_c \approx 0.1$ m/s at $y = L$, which is induced by buoyancy in the quiescent ambient condition (Fig. 6(a)). The result demonstrates that natural convection is very sensitive to perturbation by Stefan flow. This effect can be explained by the increase of thermal boundary layer thickness δ^* as the upward Stefan flow velocity increases. As shown in Fig. 5(b), δ^* increases > 5 times when Re_{V_0} increases to 240 (*i.e.*, $V_0 = 0.08$ m/s). Since the local thermal resistance is proportional to δ^*, the increase of δ^* leads to a reduction of overall heat transfer. Additionally, the FEM simulation provides more physical insight into the evolution of boundary layer (Fig. 6). Initially, the steady boundary layer (Figs. 6(a) and (d)) covers the entire plate. As the Stefan

Table 3
Summary of the inertia and conduction effect on heat transfer in different Stefan flow Reynolds number regimes.

	Expression	Behaviors at $Re_{V_0} < 50$	Behaviors at $Re_{V_0} > 150$
Inertia	$\frac{1}{105}\frac{d}{dx^*}(U^{*2}\delta^*)$	Negligible	Dominant
Conduction	$\frac{60}{Pr}$	Dominant	Negligible

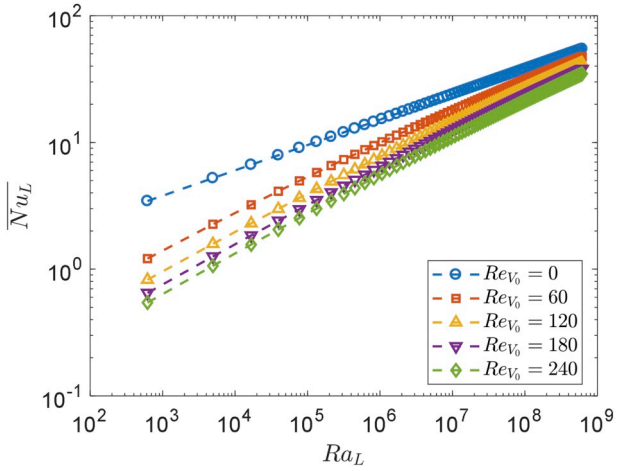

Fig. 7. Average Nusselt number $\overline{Nu_L}$ as a function of Rayleigh number Ra_L under different Stefan flow Reynolds number Re_{V_0}. The heat transfer of smaller evaporators (*i.e.*, smaller Ra_L) is more sensitive to the Stefan flow.

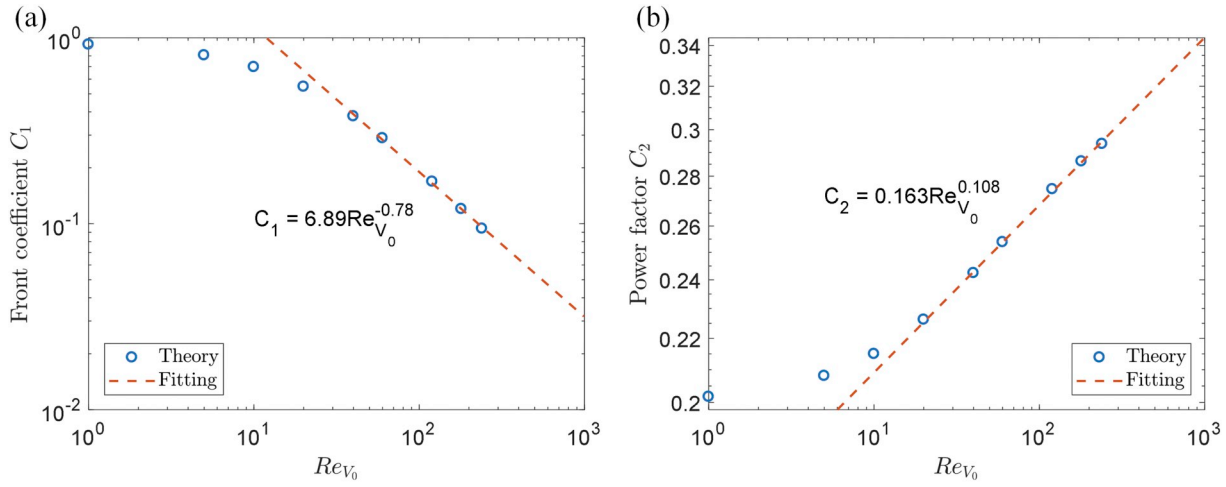

Fig. 8. (a) The coefficient C_1 and (b) the power factor C_2 as a function of Stefan flow Reynolds number Re_{V_0}. C_1 and C_2 show linear dependence with Re_{V_0} at the high Re_{V_0} regime ($Re_{V_0} > 20$) in the log-log scale, indicating C_1 and C_2 have the monomial relationship with Re_{V_0} (*i.e.*, $C_1 = 6.89{Re_{V_0}}^{-0.78}$ and $C_2 = 0.163{Re_{V_0}}^{0.108}$).

flow velocity increases, the boundary layer starts to detach from the center ($x^* = 1$, Figs. 6(b) and (e)) and finally completely separates from the evaporator (Figs. 6(c) and (f)). The boundary layer becomes very thick due to the separation (the red line in Fig. 6(d)–(f)), for which reason natural convection in high Re_{V_0} only relies on the boundary layer at the leading edge, *i.e.*, $x^* \approx 0$.

We further discuss the inertial, conductive and convective effects on the overall heat transfer at different Re_{V_0} regimes. To understand the effect of inertia and conduction, we eliminated the corresponding terms from Eqs. (12) and (13), respectively, and compared the results with the rigorous boundary layer solution (Fig. 5). We first simplified the boundary layer Eqs. (12) and (13) by neglecting the inertial term $\frac{1}{105}\frac{d}{dx^*}(U^{*2}\delta^*)$ and the conduction term $60/Pr$ (Eqs. (A.12) and (A.13) in Appendix B), which is valid at large Pr ($Pr > 1$ according to Ref. 13) and $30Re_{V_0} \gg 60/Pr$,

$$0 = -\frac{U^*}{\delta^*} + Gr_L\delta^*\frac{d\delta^*}{dx^*} \tag{20}$$

$$\frac{d}{dx^*}(U^*\delta^*) = 30Re_{V_0}. \tag{21}$$

We obtained the analytical expression for the overall heat transfer which is given by (Appendix B for detailed derivations),

$$\overline{Nu_L} = \frac{\bar{h}L}{k} = 4\left(\frac{60Re_{V_0}}{Gr_L}\right)^{-\frac{1}{4}}. \tag{22}$$

Eq. (22) clearly shows the suppression effect of Stefan flow on overall heat transfer. The average heat transfer coefficient (HTC) $\bar{h}$ decays as $Re_{V_0}^{-\frac{1}{4}}$. According to Eq. (22), however, $\overline{Nu_L}$ rises to infinity at $Re_{V_0} = 0$, because the condition $30Re_{V_0} \gg 60/Pr$ is invalid at the low Re_{V_0} regime. To describe the behavior of natural convection at low Re_{V_0}, we incorporated the term $60/Pr$ into the boundary layer equations,

$$0 = -\frac{U^*}{\delta^*} + Gr_L\delta^*\frac{d\delta^*}{dx^*} \tag{23}$$

$$\delta^*\frac{d}{dx^*}(U^*\delta^*) = 30Re_{V_0}\delta^* + \frac{60}{Pr} \tag{24}$$

and we found the mathematical expression for the boundary layer thickness,

$$4\int_0^{\delta^*}\frac{\delta^{*3}d\delta^*}{\left(\frac{240Re_{V_0}}{Gr_L}\delta^{*4} + \frac{640}{Ra_L}\delta^{*3}\right)^{\frac{1}{2}}} = x^*. \tag{25}$$

As shown in Fig. 5, $\overline{Nu_L}$ decreases to a reasonable finite value at $Re_{V_0} \approx 0$ by considering the conduction effect into Eq. (24), and $\overline{Nu_L}$ predicted by Eq. (25) converges gradually to the result given by Eq. (22) at high Re_{V_0}. Therefore, conduction through the boundary layer is the dominant effect when $Re_{V_0} < 50$, but becomes negligible as $Re_{V_0} > 150$.

We then analyzed the inertial effect by including term $\frac{1}{105}\frac{d}{dx^*}(U^{*2}\delta^*)$ into Eqs. (20) and (21), and Eqs. (23) and (24) (Eqs. (A.25), (A.26), (12) and (13)). It can be seen from Fig. 5, calculations considering the inertial term (the results of "$\overline{Nu_L}$ no Pr" and "$\overline{Nu_L}$ all" in Fig. 5(a)) agree well with the results neglecting the inertial term (the results of "$\overline{Nu_L}$ no Pr and inertia" and "$\overline{Nu_L}$ no inertia" in Fig. 5(a)) at $Re_{V_0} \approx 0$, but predict much lower overall heat transfer at large Re_{V_0}. Therefore, the inertial effect is weak when $Re_{V_0} \approx 0$ but develops to be the dominant mechanism as Re_{V_0} increases. We summarize the behavior of the conduction and inertial effects in Table 3.

To understand the sensitivity of natural convection to the Stefan flow at various evaporator sizes, we calculated the heat transfer on the evaporator from $L = 1$ cm to $L = 100$cm at various Re_{V_0} (Fig. 7). We used the same parameters listed in Table 1 and Table 2. The increase of Rayleigh number Ra_L arises from the increase of L. As shown in Fig. 7, the curve of $\overline{Nu_L}$ shifts downwards as Re_{V_0} increases due to the suppression effect. The relative change of $\overline{Nu_L}$ is less significant at larger Ra_L for the same amount change of Re_{V_0}, indicating Stefan flow induced suppression is more important for smaller evaporators. For example, when Re_{V_0} increases from 0 to 60, the natural convection heat transfer reduces by 50% for a 5 cm length evaporator while it only decreases by 20% when L is 50 cm.

From a practical consideration, it is useful to provide a correlation of $\overline{Nu_L}$ to quantify the effect of Re_{V_0} and Ra_L simultaneously. This correlation can be theoretically guided by boundary layer theory. The dependence of $\overline{Nu_L}$ on Ra_L in a log-log scale is shown in Fig. 7. The linear dependence in the log-log graph indicates that the following monomial relationship is valid,

$$\overline{Nu_L} = C_1(Re_{V_0})Ra_L^{C_2(Re_{V_0})} \tag{26}$$

where C_1 and C_2 are the front coefficient and power factor respectively, which represent the effect of Re_{V_0}. As shown in Fig. 8, the boundary layer theory can predict the relationship between these two coefficients and Re_{V_0}. We found C_1 and C_2 have good linear dependence on Re_{V_0} in the log-log scale when $Re_{V_0} > 20$. We fitted these linear coefficients and obtained the monomial correlations for C_1 and C_2,

$$C_1 = 6.89Re_{V_0}^{-0.78} \tag{27}$$

$$C_2 = 0.163Re_{V_0}^{0.108}. \tag{28}$$

Substituting Eqs. (27) and (28) into Eq. (26), we suggest a general

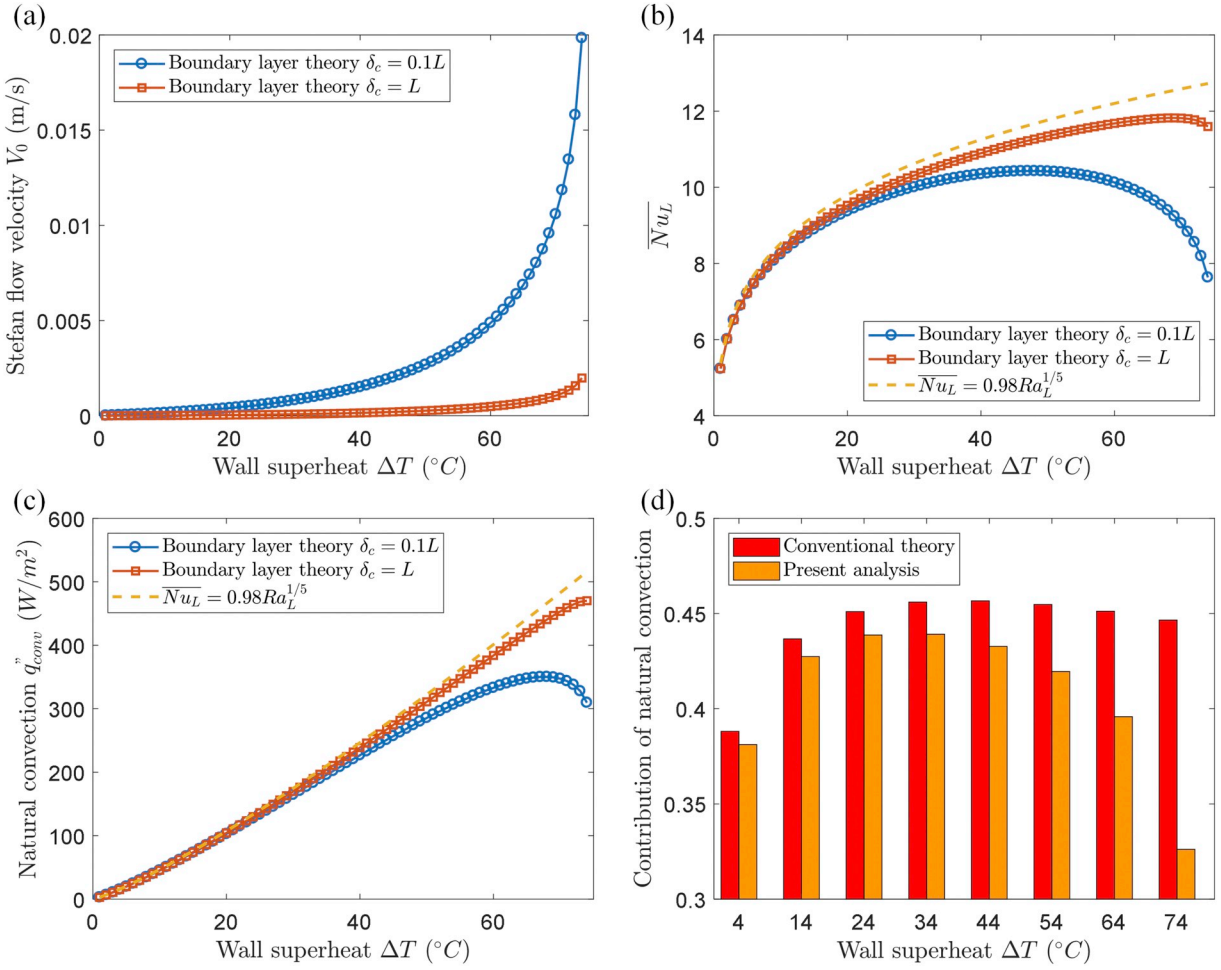

Fig. 9. Analysis of the natural convection heat loss as a function of wall superheat. (a) Stefan flow velocity V_0 as a function of wall superheat ΔT. (b) Predicted average Nusselt number $\overline{Nu_L}$ at different wall superheat ΔT. (c) Heat loss through natural convection $q_{conv}^{''}$ at different wall superheat ΔT. (d) Contribution of natural convection to the total heat loss on the evaporator varying with wall superheat ΔT.

correlation for the average Nusselt number $\overline{Nu_L}$ according to the boundary layer theory,

$$\overline{Nu_L} = 6.89 Re_{V_0}^{-0.78} Ra_L^{0.163 Re_{V_0}^{0.108}} \quad (Re_{V_0} > 20). \tag{29}$$

This correlation is valid when the Stefan flow Reynolds number Re_{V_0} is larger than 20, which can be widely used for engineering estimations.

3.3. Analysis of natural convection induced heat loss on an evaporator

In this section, we analyzed the heat loss due to natural convection on a $L = 5$ cm evaporator, which is operated at different temperatures. For an evaporator with a fixed geometrical configuration, *i.e.*, δ_c and L, the Stefan flow velocity V_0 only depends on the evaporator temperature T_s and the ambient temperature T_∞, *i.e.*, $V_0 = V_0(T_s, T_\infty)$ (Section 2.3), indicating,

$$\overline{Nu_L} = \overline{Nu_L}(Re_{V_0}, Pr, Gr_L) = \overline{Nu_L}(Re_{V_0}(\Delta T), Pr, Gr_L(\Delta T)) = \overline{Nu_L}(\Delta T) \tag{30}$$

where the average Nusselt number $\overline{Nu_L}$ then depends only on the wall superheat $\Delta T = T_s - T_\infty$ if T_∞ is fixed. We calculated the Stefan flow velocity as a function of wall superheat. We chose two representative effective diffusion boundary layer thicknesses *i.e.*, $\delta_c = 0.1L$ and $\delta_c = L$ which match different experimental conditions [28,30]. The relatively large effective diffusion boundary layer thickness is achieved by directly exposing the evaporator into a quiescent ambient, whereas the smaller diffusion boundary thickness typically occurs when the vapor at the far field removed (*i.e.*, convected) by a weak flow. As shown in Fig. 9(a), the Stefan flow velocity increases with the wall superheat, where a significant increase in V_0 occurs when T_s approaches the saturation temperature. Also, the strength of Stefan flow highly depends on the effective boundary thickness δ_c, indicating the importance of considering the Stefan flow effect for high-flux evaporators [28]. Fig. 9(b) shows the dependence of $\overline{Nu_L}$ on ΔT (Eq. (30)). At low wall superheats ΔT ($\Delta T < 30\,^\circ C$), the overall heat transfer considering the Stefan flow effect agrees well with the results in a quiescent ambient as the natural convection is in the low Re_{V_0} regime where the conduction effect (represented by $60/Pr$) is dominant (Table 3). However, the heat transfer considering the Stefan flow deviates from the quiescent ambient results when ΔT is large ($\Delta T > 30\,^\circ C$) since the Stefan flow becomes strong. For example, the average Nusselt number reduces by over 40% due to the Stefan flow effect when $\delta_c = 0.1L$ and $\Delta T = 75\,^\circ C$ (Fig. 9(b)). Consequently, it is of great interest to note that $\overline{Nu_L}$ no longer monotonically increases as ΔT increases. Instead, there is a peak value of $\overline{Nu_L}$ when the Stefan flow is strong enough, indicating that the natural convection heat transfer coefficient has a global maximum. A similar phenomenon can also be seen in the total heat loss through natural convection. As shown in Fig. 9(c), $q_{conv}^{''}$ reaches maximum 350 W/m^2 at $\Delta T \approx 67\,^\circ C$ and drops to about 300 W/m^2 when ΔT increases further (when $\delta_c = 0.1L$).

Finally, we performed heat loss analysis using the developed theory. We considered the evaporator has $\delta_c = 0.1L$ and is well-insulated. Only the radiation and natural convection contribute to the total heat loss.

We considered the evaporator has an emissivity $\varepsilon = 1$, and the contribution of natural convection to the total heat loss is expressed as q_{conv}''/q_{tot}'' where $q_{tot}'' = q_{conv}'' + q_{rad}''$. As shown in Fig. 9(d), conventional theory assuming quiescent air ambient predicts the contribution of natural convection steadily maintained at about 45% when ΔT is reasonably large because both q_{conv}'' and q_{rad}'' are scaled by ΔT in the low temperature ($T_s < 100\,^{\circ}C$) regime. However, it can be seen that the conventional theory overestimates the contribution of natural convection by ~ 40% at high ΔT, demonstrating that the Stefan flow effect needs to be carefully incorporated into the heat loss analysis of high-flux evaporators.

4. Conclusions

In this work, we identified and quantified the suppression of natural convection in an evaporation induced by Stefan flow. To understand this suppression effect, we developed a comprehensive theoretical framework which couples natural convection with the Stefan flow using boundary layer theory. The Stefan flow, which arises from the high evaporative flux of an evaporator, leads to the increase of boundary layer thickness and the reduction of convective heat transfer. This suppression effect highly relies on the Stefan flow velocity, and different heat transfer mechanisms dominate the different Stefan flow Reynolds number regimes. We found over 50% suppression of the overall natural convection is possible even though the Stefan flow is much weaker than the buoyancy-induced flow. We also considered the effect of evaporator geometry (*i.e.*, the size and effective diffusion boundary layer thickness) and wall superheat temperature on the natural convection suppression. We found that the overall heat transfer no longer monotonically increased with the wall superheat and conventional correlations significantly overestimated the heat loss through natural convection when the evaporative flux was high. We also provided a fully analytical expression of the natural convection heat loss coefficient in the presence of the Stefan flow to facilitate engineering calculations. The results presented in this study show the importance of the natural convection suppression effect to high-flux evaporators. The developed theoretical framework offers physical insights into the natural convection suppression phenomenon and can be beneficial to a wide range of applications from heat loss analysis to performance optimization of evaporators.

Appendix A. Derivation of the governing equations for natural convection in a Stefan flow

The general conservation of mass, momentum and energy equations describing fluid flow and heat transfer during natural convection are given by,

$$\frac{\partial u}{\partial x} + \frac{\partial v}{\partial y} = 0 \tag{A.1}$$

$$\rho\left(u\frac{\partial u}{\partial x} + v\frac{\partial u}{\partial y}\right) = -\frac{\partial p}{\partial x} + \mu\left(\frac{\partial^2 u}{\partial x^2} + \frac{\partial^2 u}{\partial y^2}\right) \tag{A.2}$$

$$\rho\left(u\frac{\partial v}{\partial x} + v\frac{\partial v}{\partial y}\right) = -\frac{\partial p}{\partial y} - \rho_\infty(1 - \beta(T - T_\infty))g + \mu\left(\frac{\partial^2 v}{\partial x^2} + \frac{\partial^2 v}{\partial y^2}\right) \tag{A.3}$$

$$u\frac{\partial T}{\partial x} + v\frac{\partial T}{\partial y} = \alpha\left(\frac{\partial^2 T}{\partial x^2} + \frac{\partial^2 T}{\partial y^2}\right). \tag{A.4}$$

To simplify the governing equations, we considered the following dimensionless variables,

$$u^* = \frac{u}{U},\ v^* = \frac{v}{V_0},\ x^* = \frac{x}{L},\ y^* = \frac{y}{\delta},\ and\ p^* = \frac{p}{\rho_\infty U^2} \tag{A.5}$$

where $L \gg \delta$. According to the governing Eqs. (A.1) to (A.4), we have the scaling analysis on the order of magnitude estimation for each term. The continuity equation gives,

$$\frac{\partial u}{\partial x} + \frac{\partial v}{\partial y} = 0 \rightarrow \frac{U}{L} \sim \frac{V_0}{\delta}. \tag{A.6}$$

Substituting Eqs. (A.5) and (A.6) into the x-momentum Eq. (A.2),

$$\begin{aligned}
\rho u\tfrac{\partial u}{\partial x} &\sim \tfrac{\rho U^2}{L},\\
\rho v\tfrac{\partial u}{\partial y} &\sim \tfrac{\rho U^2}{L},\\
\tfrac{\partial p}{\partial x} &\sim \tfrac{\rho U^2}{L},\\
\mu\tfrac{\partial^2 u}{\partial x^2} &\sim \tfrac{\mu U}{L^2},\\
\mu\tfrac{\partial^2 u}{\partial y^2} &\sim \tfrac{\mu U}{\delta^2}.
\end{aligned} \tag{A.7}$$

As $\mu U^2/\delta^2 \gg \mu U^2/L^2$, the x-momentum equation can be simplified as,

$$\rho\left(u\frac{\partial u}{\partial x} + v\frac{\partial u}{\partial y}\right) = -\frac{\partial p}{\partial x} + \mu\frac{\partial^2 u}{\partial y^2}. \tag{A.8}$$

Similarly, in the y-momentum equation, we have the following scaling terms,

$$\begin{aligned}
\rho u\frac{\partial v}{\partial x} &\sim \frac{\rho U^2\delta}{L^2},\\
\rho v\frac{\partial v}{\partial y} &\sim \frac{\rho U^2\delta}{L^2},\\
\frac{\partial p}{\partial y} &\sim \frac{\rho U^2}{\delta},\\
\mu\frac{\partial^2 v}{\partial x^2} &\sim \frac{\mu U\delta}{L^3},\\
\mu\frac{\partial^2 v}{\partial y^2} &\sim \frac{\mu U}{\delta L}.
\end{aligned} \tag{A.9}$$

The pressure term ($\rho U^2/\delta$) is much larger than the inertial term ($\rho U^2\delta/L^2$) since $L \gg \delta$. In addition, the viscous term can also be neglected when $Re_U \gg 1$. Consequently, the y-momentum equation can be expressed as,

$$\rho_\infty(1-\beta(T-T_\infty))g = -\frac{\partial p}{\partial y}. \tag{A.10}$$

In Eq. (A.4), the heat conduction along x-direction can be neglected since $L \gg \delta$, for which reason the energy equation is simplified as,

$$u\frac{\partial T}{\partial x} + v\frac{\partial T}{\partial y} = \alpha\frac{\partial^2 T}{\partial y^2}. \tag{A.11}$$

Appendix B. Solutions to the boundary layer equations

We firstly solved the boundary layer Eqs. (12) and (13) neglecting the inertial term $\frac{1}{105}\frac{d}{dx^*}(U^{*2}\delta^*)$ and the conduction term $60/Pr$ when the Stefan flow Reynolds number Re_{V_0} and Prandtl number Pr are large, *i.e.*, $30Re_{V_0} \gg 60/Pr$. The simplified boundary layer equations are given by,

$$0 = -\frac{U^*}{\delta^*} + Gr_L\delta^*\frac{d\delta^*}{dx^*} \tag{A.12}$$

$$\frac{d}{dx^*}(U^*\delta^*) = 30Re_{V_0}. \tag{A.13}$$

According to Eq. (A.13), we had,

$$U^*\delta^* = 30Re_{V_0}x^*. \tag{A.14}$$

Substituting Eq. (A.14) into Eq. (A.12) and eliminating U^*, we obtained,

$$\frac{30Re_{V_0}}{Gr_L}x^*dx^* = \delta^{*3}d\delta^*. \tag{A.15}$$

Integrating Eq. (A.15) on both sides, we obtained the boundary layer thickness,

$$\delta^* = \left(\frac{60Re_{V_0}}{Gr_L}\right)^{\frac{1}{4}}x^{*\frac{1}{2}}, \tag{A.16}$$

and the average Nusselt number is given by,

$$\overline{Nu_L} = \frac{\bar{h}L}{k} = 4\left(\frac{60Re_{V_0}}{Gr_L}\right)^{-\frac{1}{4}}. \tag{A.17}$$

We next considered the more rigorous solution by including conduction contribution but still neglecting the inertial effect,

$$0 = -\frac{U^*}{\delta^*} + Gr_L\delta^*\frac{d\delta^*}{dx^*} \tag{A.18}$$

$$\delta^*\frac{d}{dx^*}(U^*\delta^*) = 30Re_{V_0}\delta^* + \frac{60}{Pr}. \tag{A.19}$$

Plugging Eq. (A.18) into Eq. (A.19) and eliminating term U^*, we obtained,

$$\delta^*\frac{d}{dx^*}\left(\frac{d\delta^{*4}}{dx^*}\right) = \frac{120Re_{V_0}}{Gr_L}\delta^* + \frac{240}{Ra_L}. \tag{A.20}$$

We used the following transformation and substituted it into Eq. (A.20),

$$\phi = \frac{d\delta^{*4}}{dx^*},\ where\ \phi\frac{d\phi}{d\delta^*} = \frac{d\phi}{dx^*} = \frac{d}{dx^*}\left(\frac{d\delta^{*4}}{dx^*}\right), \tag{A.21}$$

and

$$\phi d\phi = \frac{120Re_{V_0}}{Gr_L}d\delta^{*4} + \frac{240}{Ra_L}\frac{d\delta^{*4}}{\delta^*}. \tag{A.22}$$

Integrating Eq. (A.22) on both sides and considering $d\delta^*/dx^* \approx 0$ at $x^* = 1$ (flat boundary layer assumption), we obtained the differential equation for the boundary layer thickness,

$$\phi = \frac{d\delta^{*4}}{dx^*} = \left(\frac{240Re_{V_0}}{Gr_L}\delta^{*4} + \frac{640}{Ra_L}\delta^{*3}\right)^{\frac{1}{2}}. \tag{A.23}$$

Eq. (A.23) gives the implicit form of the boundary layer thickness,

$$4\int_0^{\delta^*} \frac{\delta^{*3}d\delta^*}{\left(\frac{240Re_{V_0}}{Gr_L}\delta^{*4} + \frac{640}{Ra_L}\delta^{*3}\right)^{\frac{1}{2}}} = x^*. \tag{A.24}$$

To consider the effect of the inertial term in the boundary layer equations, numerical solutions are required. The differential equations including the inertial term but still neglecting the conduction term are given by,

$$\frac{1}{105}\frac{d}{dx^*}(U^{*2}\delta^*) = -\frac{U^*}{\delta^*} + Gr_L\delta^*\frac{d\delta^*}{dx^*} \tag{A.25}$$

$$\frac{d}{dx^*}(U^*\delta^*) = 30Re_{V_0}. \tag{A.26}$$

Still, substituting Eq. (A.26) into Eq. (A.25) and eliminating term U^*, we obtained,

$$\frac{d\delta^*}{dx^*} = \frac{\frac{120}{7}Re_{V_0}^2x^*\delta^* + 30Re_{V_0}x^*}{Gr_L\delta^{*3} + \frac{60}{7}Re_{V_0}^2x^{*2}} = f(x^*, \delta^*) \tag{A.27}$$

which was solved numerically using *ode45* in MATLAB.

Finally, we solved the boundary layer Eqs. (12) and (13) rigorously considering all terms. Denoting $a = U^{*2}\delta^*$ and $b = U^*\delta^*$, Eqs. (12) and (13) can be rearranged as,

$$\frac{da}{dx^*} = \frac{-\frac{a^2}{b^3} + Gr_L\frac{2b^3}{a^2}\left(30Re_{V_0} + \frac{60}{Pr}\frac{a}{b^2}\right)}{\frac{1}{105} + Gr_L\frac{b^4}{a^3}} = f_1(a,b) \tag{A.28}$$

$$\frac{db}{dx^*} = 30Re_{V_0} + \frac{60}{Pr}\frac{a}{b^2} = f_2(a,b) \tag{A.29}$$

with initial conditions $a|_{x^*=0} = b|_{x^*=0} = 0$. Similarly, Eqs. (A.28) and (A.29) can be solved by *ode45* using MATLAB.

Appendix C. Extra considerations: the vertical boundary layer in region II

In this section, we solved the vertical boundary layer (region II in Fig. 2). We simplified the governing equations (Eqs. (A.1) and (A.4)) using the dimensionless variables $x^* = x/\delta_v$ and $y^* = y/H$ where $H \gg \delta_v$ is the characteristic length scale in vertical direction. Performing similar scaling analysis, we obtained the following equations,

$$\frac{\partial u}{\partial x} + \frac{\partial v}{\partial y} = 0 \tag{A.30}$$

$$0 = -\frac{\partial p}{\partial x} \tag{A.31}$$

$$u\frac{\partial v}{\partial x} + v\frac{\partial v}{\partial y} = g\beta(T - T_\infty) + \nu\frac{\partial^2 v}{\partial x^2} \tag{A.32}$$

$$u\frac{\partial T}{\partial x} + v\frac{\partial T}{\partial y} = \alpha\frac{\partial^2 T}{\partial x^2}. \tag{A.33}$$

We assumed the velocity and temperature profile,

$$v(x,y) = V(y)\left(\frac{x}{\delta_v(y)} - 1\right)^2\left(\frac{2x}{\delta_v(y)} + 1\right) \tag{A.34}$$

$$\frac{T(x,y) - T_\infty}{T_s - T_\infty} = \left(\frac{x}{\delta_v(y)} - 1\right)^2\left(\frac{2x}{\delta_v(y)} + 1\right) \tag{A.35}$$

where $V(y = 0) = V_0$. We obtained the vertical boundary layer equations by performing similar integral within the boundary layer and substituting Eqs. (A.34) and (A.35) into corresponding integral equations,

$$\frac{13}{35}\frac{d}{dy}(V^2\delta_v) = \frac{1}{2}g\beta\Delta T\delta_v \tag{A.36}$$

$$\frac{d}{dy}(V\delta) = 0. \tag{A.37}$$

Eq. (A.37) indicates $V\delta = V\delta|_{y=0} \approx V_0L$. Plugging Eq. (A.37) into Eq. (A.36), we solved the vertical boundary layer as,

$$\delta_v^* = \frac{\delta_v}{L} = \left(1 + \frac{70}{26}\frac{Gr_L}{Re_{V_0}^2}y^*\right)^{-\frac{1}{2}} \tag{A.38}$$

where the $y^* = y/L$ in Eq. (A.38). According to Eqs. (A.37) and (A.38), the vertical flow velocity is given by,

$$V(y) = V_0\left(1 + \frac{70}{26}\frac{\beta g \Delta T}{V_0^2 L^2}y\right)^{\frac{1}{2}}. \tag{A.39}$$

It can be seen from Eq. (A.39) that the air flow is accelerated due to the buoyant force. The vertical boundary thickness decreases accordingly to conserve the mass in boundary layer, which agrees well with the COMSOL simulation.

Appendix D. Details of the finite element simulation

In this section, we verified that the numerical results of the finite element simulations are mesh independent and domain size independent. For this purpose, we simulated the evaporator heat flux subject to pure natural convection (*i.e.,* without the induced Stefan flow). The evaporator temperature was fixed at $T_s = 40\,^{\circ}C$ and the ambient temperature was $T_\infty = 25\,^{\circ}C$. The half evaporator length was $L = 5$ cm. Fig. A1(a) shows the evaporator heat flux as a function of the leading edge mesh refinement factor (*i.e.*, number of mesh points within $0.2L$ of the leading edge, see inset). When the mesh was coarse, the simulation severely overestimated the evaporator heat flux. After increasing the refinement factor above 50, the heat flux converged to its true value. Fig. A1(b) shows the dependence on the simulation domain size. The domain size was measured in terms of the half evaporator length L. It turned out that the simulation results were not sensitive to the choice of domain size. For the simulations carried out in this study, we chose a refinement factor of 100 and a domain size of $2.5L$ considering both accuracy and computational cost.

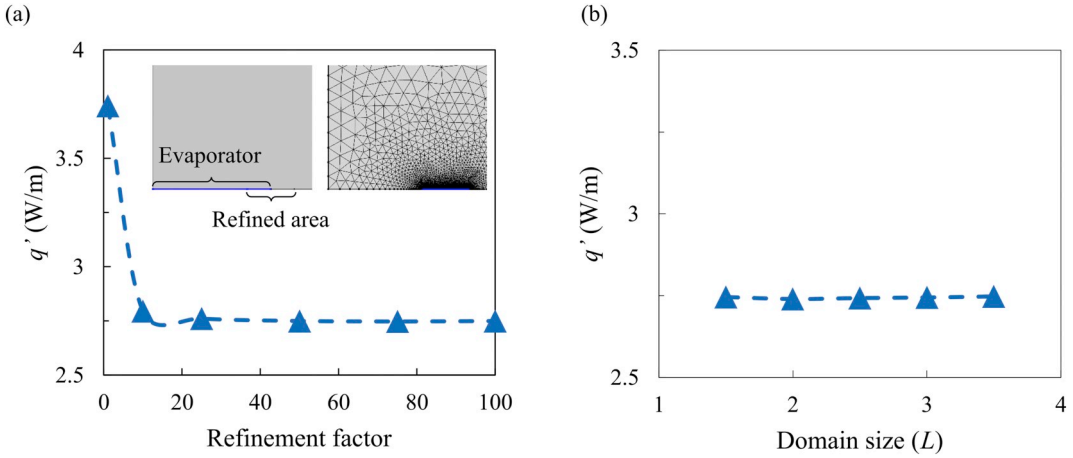

Fig. A1. (a) Evaporator heat flux as a function of the refinement factor. Inset: detailed view of the evaporator in the simulation domain (left), and refined mesh near the evaporator leading edge (right). (b) Evaporator heat flux as a function of the simulation domain size (L – the half evaporator length).

Appendix E. Comparison between the boundary layer theory and FEM results

In this section, we compared the results from boundary layer theory and FEM and discussed the sources of discrepancy. Fig. A2 shows the local heat transfer coefficient (HTC) as a function of x position under different Stefan flow velocities. When $V_0 = 0$ m/s, the result of boundary layer theory agrees with that of the FEM very well in general. However, small discrepancies were found at the leading edge ($x \to 0$ mm) and center of the evaporator ($x \to 50$ mm), which indicate two sources of deviation (the inset of Fig. A2(a)). Specifically, the discrepancy at the leading edge arises from the mesh refinement of numerical calculation. Note $x = 0$ mm is a singular point with zero boundary layer thickness and infinitively large local HTC, and most of the heat transfer occurs at the leading edge region. To accurately predict the heat transfer, extra refinement of mesh at the leading edge should be carried out. Boundary layer theory is computationally efficient, which enables very good refinement at the leading edge (~ 0.001 mm between two neighboring nodes), whereas the corresponding refinement of FEM (length between two nearest nodes) is 0.1 mm. For this reason, the maximum HTC at $x = 0$ mm from our boundary layer theory can reach $\sim 1100\,\mathrm{W/m^2K}$, but the corresponding HTC at the same position from FEM is only $\sim 100\,\mathrm{W/m^2K}$. This poor spatial resolution in the mesh of FEM can lead to an underestimation of $\overline{Nu_L}$. The second discrepancy shown in the middle of the evaporator (the inset of Fig. A2(a)) attributes to the assumption of boundary layer theory. Since boundary separation occurs at the region II (Fig. 2) which is not considered by the boundary layer theory, it overestimates the local HTC at the center. Because of these two sources of discrepancy, the boundary layer theory can always predict $\overline{Nu_L}$ to be higher than FEM (Fig. 4(a)). When V_0 increases to 0.02 m/s and 0.08 m/s, although the local HTC predicted by the boundary layer theory still agrees with that of the FEM well (Fig. A2(b) and (c)), a larger discrepancy was observed at the leading edge region due to both the numerical resolution and the boundary separation (the insets of Fig. A2(b) and (c)). However, the discrepancy at the center becomes very small (the insets of Figs. A2(b) and (c)) because the boundary layer is very thick at large Re_{V_0} (Figs. 5(b) and 6). Therefore, compared to the FEM, the boundary layer theory provides a relatively conservative prediction for the natural convection suppression effect.

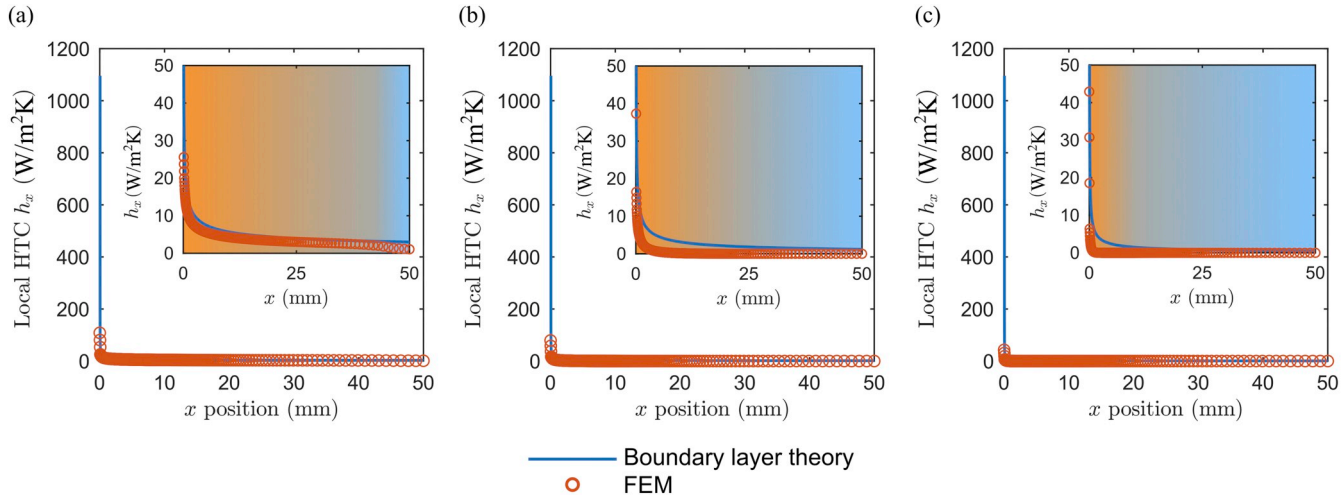

Fig. A2. Local HTC h_x calculated by the boundary layer theory (blue line) and FEM simulation (red open circle) for (a) V_0 = 0 m/s (Re_{V_0} = 0), (b) V_0 = 0.02 m/s (Re_{V_0}~60) and (c) V_0 = 0.08 m/s (Re_{V_0}~240). The inset shows a zoom-in view of the HTC near the leading edge. The orange shaded area indicates where the dominant heat transfer occurs (x = 0 mm indicates the leading edge). (For interpretation of the references to colour in this figure legend, the reader is referred to the web version of this article.)

Nomenclature

D	mass diffusivity (m^2/s)
T_∞	far field temperature (K)
g	gravity constant (m/s^2)
ΔT	wall superheat (K)
Gr_L	Grashof number
u	flow velocity at x-direction (m/s)
h_x	local heat transfer coefficient (W/(m^2·K))
U	bulk flow velocity at x-direction (m/s)
$\overline{h}$	average heat transfer coefficient (W/(m^2·K))
v	flow velocity at y-direction (m/s)
j	vapor mass flux (kg/(m^2·s))
V_0	Stefan flow velocity (m/s)
k	thermal conductivity (W/(m·K))
V_c	Characteristic vertical flow velocity (m/s)
L	evaporator half length (m)
x	x coordinate (m)
M_v	water molecular weight (kg/mol)
x^*	dimensionless x coordinate
$\overline{Nu_L}$	average Nusselt number
y	y coordinate (m)
p	pressure (Pa)
y^*	dimensionless y coordinate
p_∞	far field pressure (Pa)

Greek letters

p_v	vapor pressure (Pa)
α	thermal diffusivity (m^2/s)
$p_{v,\infty}$	vapor pressure at far field (Pa)
β	coefficient of thermal expansion (1/K)
$p_{v,s}$	vapor pressure on the substrate (Pa)
δ	boundary layer thickness (m)
Pr	Prandtl number
δ^*	dimensionless boundary layer thickness
R_0	specific gas constant (J/(kg·K))
δ_c	effective diffusive boundary layer thickness
Ra_L	Rayleigh number
ε	emissivity
Re_{V_0}	Stefan flow Reynolds number
μ	dynamic viscosity (Pa·s)

T	temperature (K)
ν	kinematic viscosity (m^2/s)
T_f	film temperature (K)
ρ	gas density (kg/m^3)
T_s	substrate temperature (K)
ρ_∞	far field gas density (kg/m^3)

References

[1] T.W. Kenny, K.E. Goodson, J.G. Santiago, E. Wang, J. Koo, L. Jiang, E. Pop, S. Sinha, L. Zhang, D. Fogg, S. Yao, R. Flynn, C. Chang, C.H. Hidrovo, Advanced cooling technologies for microprocessors, Int. J. High Speed Electron. Syst. 16 (2006) 301–313, https://doi.org/10.1142/S0129156406003655.

[2] S. Adera, D.S. Antao, R. Raj, E.N. Wang, Hotspot thermal management via thin-film evaporation – part I: experimental characterization, IEEE Trans. Components, Packag. Manuf. Technol. 8 (2018) 88–98, https://doi.org/10.1109/TCPMT.2017.2757463.

[3] S. Adera, D.S. Antao, R. Raj, E.N. Wang, Hotspot thermal management via thin-film evaporation—part II: modeling, IEEE Trans. Components, Packag. Manuf. Technol. 8 (2018) 99–112, https://doi.org/10.1109/TCPMT.2017.2757461.

[4] K.L. Wilke, B. Barabadi, Z. Lu, T. Zhang, E.N. Wang, Parametric study of thin film evaporation from nanoporous membranes, Appl. Phys. Lett. 111 (2017), https://doi.org/10.1063/1.4997945.

[5] F. Zhao, X. Zhou, Y. Shi, X. Qian, M. Alexander, X. Zhao, S. Mendez, R. Yang, L. Qu, G. Yu, Highly efficient solar vapour generation via hierarchically nanostructured gels, Nat. Nanotechnol. 13 (2018) 489–495, https://doi.org/10.1038/s41565-018-0097-z.

[6] G. Ni, S.H. Zandavi, S.M. Javid, S.V. Boriskina, T.A. Cooper, G. Chen, A salt-rejecting floating solar still for low-cost desalination, Energy Environ. Sci. 11 (2018) 1510–1519, https://doi.org/10.1039/c8ee00220g.

[7] G. Ni, G. Li, S.V.V. Boriskina, H. Li, W. Yang, T.J. Zhang, G. Chen, Steam generation under one sun enabled by a floating structure with thermal concentration, Nat. Energy 1 (2016) 16126, , https://doi.org/10.1038/nenergy.2016.126.

[8] H. Ghasemi, G. Ni, A.M. Marconnet, J. Loomis, S. Yerci, N. Miljkovic, G. Chen, Solar steam generation by heat localization, Nat. Commun. 5 (2014) 4449, , https://doi.org/10.1038/ncomms5449.

[9] L. Zhou, Y. Tan, J. Wang, W. Xu, Y. Yuan, W. Cai, S. Zhu, J. Zhu, 3D self-assembly of aluminium nanoparticles for plasmon-enhanced solar desalination, Nat. Photonics 10 (2016) 393–398, https://doi.org/10.1038/nphoton.2016.75.

[10] T. Li, H. Liu, X. Zhao, G. Chen, J. Dai, G. Pastel, C. Jia, C. Chen, E. Hitz, D. Siddhartha, R. Yang, L. Hu, Scalable and highly efficient mesoporous wood-based solar steam generation device: localized heat, rapid water transport, Adv. Funct. Mater. 28 (2018) 1–8, https://doi.org/10.1002/adfm.201707134.

[11] A.F. Mills, Heat Transfer, Prentice Hall, 1999.

[12] Z. Rotem, L. Claassen, Natural convection above unconfined horizontal surfaces, J. Fluid Mech. 39 (1969) 173–192, https://doi.org/10.1017/S0022112069002102.

[13] J.V. Clifton, A.J. Chapman, Natural-convection on a finite-size horizontal plate, Int. J. Heat Mass Transf. 12 (1969) 1573–1584, https://doi.org/10.1016/0017-9310(69)90092-1.

[14] T. Fujii, H. Imura, Natural-convection heat transfer from a plate with arbitrary inclination, Int. J. Heat Mass Transf. 15 (1972) 755–767, https://doi.org/10.1016/0017-9310(72)90118-4.

[15] J.J. Wei, B. Yu, Y. Kawaguchi, Simultaneous natural-convection heat transfer above and below an isothermal horizontal thin plate, Numer. Heat Transf. Part A. 44 (2003) 39–58, https://doi.org/10.1080/713838175.

[16] I. Martorell, J. Herrero, F.X. Grau, Natural convection from narrow horizontal plates at moderate Rayleigh numbers, Int. J. Heat Mass Transf. 46 (2003) 2389–2402, https://doi.org/10.1016/S0017-9310(03)00010-3.

[17] D. Venturi, B. Pulvirenti, S. Salvigni, Direct numerical simulation of natural convection over horizontal plates, Lloydia (Cincinnati). (2005) 20–22.

[18] S. Samanta, A. Guha, A similarity theory for natural convection from a horizontal plate for prescribed heat flux or wall temperature, Int. J. Heat Mass Transf. 55 (2012) 3857–3868, https://doi.org/10.1016/j.ijheatmasstransfer.2012.02.031.

[19] L. Fontana, Free convention heat transfer from an isothermal horizontal thin strip: the influence of the Prandtl number, J. Therm. Sci. 23 (2014) 586–592, https://doi.org/10.1007/s11630-014-0745-z.

[20] A. Guha, K. Pradhan, A unified integral theory of laminar natural convection over surfaces at arbitrary inclination from horizontal to vertical, Int. J. Therm. Sci. 111 (2017) 475–490, https://doi.org/10.1016/j.ijthermalsci.2016.08.011.

[21] K.H. Lin, C.C. Liao, S.Y. Lien, C.A. Lin, Thermal lattice Boltzmann simulations of natural convection with complex geometry, Comput. Fluids 69 (2012) 35–44, https://doi.org/10.1016/j.compfluid.2012.08.012.

[22] V.M. Soundalgekar, P.D. Wavre, Unsteady free convection flow past an infinite vertical plate with constant suction and mass transfer, Int. J. Heat Mass Transf. 20 (1977) 1363–1373, https://doi.org/10.1016/0017-9310(77)90033-3.

[23] M.A. Hossain, M.A. Alim, D.A.S. Rees, The effect of radiation on free convection from a porous vertical plate, Int. J. Heat Mass Transf. 42 (1998) 181–191, https://doi.org/10.1016/S0017-9310(98)00097-0.

[24] M. Alam, M. Rahman, M. Samad, Dufour and Soret effects on unsteady MHD free convection and mass transfer flow past a vertical porous plate in a porous medium, Nonlinear Anal. Model. Control. 11 (2006) 217–226, https://doi.org/10.3329/jname.v2i1.2030.

[25] O.D. Makinde, Free convection flow with thermal radiation and mass transfer past a moving vertical porous plate, Int. Commun. Heat Mass Transf. 32 (2005) 1411–1419, https://doi.org/10.1016/j.icheatmasstransfer.2005.07.005.

[26] C.H. Chen, Heat and mass transfer in MHD flow by natural convection from a permeable, inclined surface with variable wall temperature and concentration, Acta Mech. 172 (2004) 219–235, https://doi.org/10.1007/s00707-004-0155-5.

[27] T.S. Chen, W.P. Buchanan, B.F. Armaly, Natural convection on vertical and horizontal plates with vectored surface mass transfer, Int. J. Heat Mass Transf. 36 (1993) 479–487, https://doi.org/10.1016/0017-9310(93)80023-N.

[28] Z. Lu, K.L. Wilke, D.J. Preston, I. Kinefuchi, E. Chang-Davidson, E.N. Wang, An ultrathin nanoporous membrane evaporator, Nano Lett. 17 (2017) 6217–6220, https://doi.org/10.1021/acs.nanolett.7b02889.

[29] R.B. Bird, E.N. Lightfoot, E.W. Stewart, Transport Phenomenon, Wiley, 2007.

[30] L. Zhang, Y. Zhu, Z. Lu, L. Zhao, K.R. Bagnall, S.R. Rao, E.N. Wang, Characterization of thin film evaporation in micropillar wicks using micro-Raman spectroscopy, Appl. Phys. Lett. 113 (2018) 163701, , https://doi.org/10.1063/1.5048837.

[31] M. Corcione, Heat transfer correlations for free convection from upward-facing horizontal rectangular surfaces, WSEAS Trans. Heat Mass Transf. 2 (2007) 48–60 http://wseas.us/e-library/transactions/heat/2007/25-637N.pdf.

[32] T.S. Chen, K.L. Tzuoo, Vortex instability of free convection flow over horizontal and inclined surfaces, J. Heat Transf. 104 (1982) 637, https://doi.org/10.1115/1.3245179.

[33] H.C. Tien, T.S. Chen, B.F. Armaly, Wave instability of natural convection flow on inclined flat plates with uniform surface heat flux, Numer. Heat Transf. 10 (1986) 179–193, https://doi.org/10.1080/10407788608913515.